

A shared law between sources of repeating fast radio bursts

Mohammed A. Chamma,¹[★] Fereshteh Rajabi,^{2,3} Christopher M. Wyenberg,¹
Abhilash Mathews⁴ and Martin Houde¹[†]

¹Department of Physics and Astronomy, The University of Western Ontario, 1151 Richmond Street, London, Ontario N6A 3K7, Canada

²Perimeter Institute for Theoretical Physics, Waterloo, ON N2L 2Y5, Canada

³Institute for Quantum Computing and Department of Physics and Astronomy, The University of Waterloo, 200 University Ave. West, Waterloo, Ontario N2L 3G1, Canada

⁴Plasma Science and Fusion Center, Massachusetts Institute of Technology, 77 Massachusetts Avenue, Cambridge, MA 02139, USA

ABSTRACT

We study the spectro-temporal characteristics of two repeating fast radio bursts (FRBs), namely, FRB 180916.J0158+65 and FRB 180814.J0422+73, and combine the results with those from our earlier analysis on FRB 121102. The relationship between the frequency drift rate of individual sub-bursts and their temporal duration is investigated. **We consider a generous range of possible DMs for each source to understand the range of valid drift rate and duration measurements for each burst and to constrain our results. Within these constraints we find good agreement with** an inverse scaling law between the two parameters previously predicted using a simple dynamical relativistic model for all sources. The remarkably similar behavior observed in all sources provides strong evidence that a single and common underlying physical phenomenon is responsible for the emission of signals from these three FRBs, despite their associations with different types of host galaxies at various redshifts. It also opens up the possibility that this sub-burst drift law may be a universal property among repeating FRBs, or at least for a significant subclass among them.

Key words: radiation: dynamics – relativistic processes – radiation mechanisms: non-thermal

1 INTRODUCTION

Fast radio bursts are short duration (\sim millisecond) bursts of energy at radio wavelengths exhibiting large brightness temperatures ($T_B > 10^{32}$ K; Lorimer et al. 2007; Petroff et al. 2019), indicating that these signals originate from non-thermal objects through some coherent emission mechanism. Still, the origin and underlying physical mechanism of FRBs remain unknown in spite of the large number of proposed models. FRB signals also undergo a high level of dispersion as they propagate from the source to the observer, a phenomenon quantified through the dispersion measure (DM). This dispersion results from the wavelength dependence of the refractive index of ionized matter in astronomical media through which radiation travels at varying speeds as a function of frequency. While a first Galactic FRB was recently reported by the CHIME/FRB Collaboration and the STARE2 team toward the Galactic magnetar SGR 1935+2154 (The CHIME/FRB Collaboration et al. 2020; Bochenek et al. 2020; Kirsten et al. 2020), the DM values measured for most FRBs suggest that these signals must emanate from extragalactic sources.

Reported FRBs fall into two groups: one-off events and re-

peaters. While one-off events form the majority of detections, most of our knowledge about FRBs is based on the study of repeaters. At the time of writing, two repeaters (FRB 121102 and FRB 180916.J0158+65) show periodic behaviours, prompting continued follow-up observations (CHIME/FRB et al. 2020; Rajwade et al. 2020). Importantly, the study of dynamic spectra of repeaters reveals interesting patterns. Among these are a downward drift in the central frequency of consecutive sub-bursts with increasing arrival time within an event (the so-called “sad trombone” effect), and a reduction in the temporal duration of individual sub-bursts with increasing frequency (Gajjar et al. 2018; Hessels et al. 2019; CHIME/FRB et al. 2019; Joseph et al. 2019).

Several models have been proposed to explain these spectro-temporal characteristics. Some models link these characteristics to the intrinsic radiation mechanism of FRBs (Wang et al. 2019; Beloborodov 2020; Metzger et al. 2019) or propagation effects (e.g., plasma lensing (Cordes et al. 2017) or scintillation (Simard & Ravi 2020)), while others argue that a combination of both factors can play a part (Hessels et al. 2019). Recently, the detection of the first Galactic FRB (The CHIME/FRB Collaboration et al. 2020; Bochenek et al. 2020; Kirsten et al. 2020) has posed new challenges for existing theoretical models. For example, one sequence of sub-bursts detected toward this source reveals an upward central frequency drift with increasing arrival time (a “happy trombone”

[★] E-mail: mchamma@uwo.ca

[†] E-mail: mhoude2@uwo.ca

effect). A few models have anticipated such a possibility for the spectra of FRBs (Simard & Ravi 2020; Rajabi et al. 2020; Beniamini & Kumar 2020). In particular, in Rajabi et al. (2020) we proposed a simple dynamical relativistic model where a descending or an ascending central frequency drift for a sequence of sub-bursts can be explained based on the intrinsic properties of the corresponding FRB source (as discussed in sections 5-5.1). But more importantly, our model also predicts that a steeper frequency drift should be present within individual sub-bursts (henceforth the sub-burst drift) where the slope of the FRB signal as displayed in a dynamical spectrum (i.e., frequency vs. time) obeys a simple law scaling inversely with the temporal duration of the sub-burst. We further provided evidence for this sub-burst drift behavior for FRB 121102 and showed that data taken over a wide range of frequencies for this repeater follows the same law, i.e., the aforementioned inverse scaling of the sub-bursts drift with their corresponding temporal duration. We then argued that this finding implies that the underlying physical process responsible for the signals detected in FRB 121102 is intrinsically narrow-band in nature, while relativistic motions within the source are required to explain the wide observed bandwidths. In this paper, we examine data from two additional repeaters, FRB 180814.J0422+73 (CHIME/FRB et al. 2019) and FRB 180916.J0158+65 (CHIME/FRB Collaboration et al. 2019; CHIME/FRB et al. 2020), and show that this form of law is closely shared between these three FRBs originating from host galaxies at different redshifts. We also consider the effect of the chosen DM on the measurements of the sub-burst drift rate and the burst duration in order to understand the robustness of this relationship between the sources. This significant finding reveals new insights on the underlying physical mechanism at the source of FRB signals and helps refine modelling efforts.

1.1 Triggered Dynamical Model

In Rajabi et al. (2020) we introduced a simple dynamical model where a triggering source (e.g., a pulsar or magnetar; see Houde et al. 2019) is located directly behind an FRB source as seen by an observer. The regions from which FRB signals are emanating are assumed to be moving towards (or away from) the observer, potentially at relativistic speeds. Such a scenario is appropriate for situations where the emitted signal is highly collimated, such as is the case for a radiation process based on Dicke's superradiance which our proposed FRB model is ultimately inspired by (Rajabi & Houde 2016a,b; Rajabi & Houde 2017; Mathews 2017; Houde et al. 2018; Houde et al. 2019; Rajabi et al. 2019; Rajabi & Houde 2020). Under such conditions we showed that the sub-burst drift from a single FRB signal (for repeaters an event can contain several sub-bursts) obeys the following relation

$$\frac{1}{\nu_{\text{obs}}} \frac{d\nu_{\text{obs}}}{dt_{\text{D}}} = -\frac{A}{t_{\text{w}}}, \quad (1)$$

where ν_{obs} , t_{w} and t_{D} are the frequency, the temporal duration of the FRB sub-burst and the delay before its appearance (in relation to the arrival of the trigger) as measured by the observer. The systemic parameter $A \equiv \tau'_{\text{w}}/\tau'_{\text{D}}$ with τ'_{w} and τ'_{D} the corresponding sub-burst proper temporal duration and delay in the FRB reference frame, respectively.

2 BURST ANALYSIS

Although equation (1) was tested and verified for FRB 121102 in Rajabi et al. (2020) using previously published data covering more than a decade in frequency (Michilli et al. 2018; Gajjar et al. 2018; Josephy et al. 2019), it was not known at the time whether it applies equally well to other repeating FRBs. We therefore retrieved and analyzed previously published data for two other sources discovered by the CHIME/FRB Collaboration (Fonseca et al. 2020), namely FRB 180916.J0158+65 (CHIME/FRB et al. 2020) and FRB 180814.J0422+73 (CHIME/FRB et al. 2019). These data are all contained within the CHIME/FRB spectral band (approximately 400–800 MHz) and the corresponding dynamic spectra were analyzed using the two-dimensional autocorrelation technique introduced in Hessels et al. (2019), resulting in estimates for the sub-burst drift ($d\nu_{\text{obs}}/dt_{\text{D}}$) and temporal duration (t_{w}); see section 4 for more details. These data sources were chosen purely due to their ease of accessibility and the support available, and other sources are not included due to difficulties in accessing and handling. Ultimately we aim to extend this analysis to as many sources as possible.

2.1 Effect of Dispersion Measure (DM)

Since the measurement of any drift rate (or almost any other spectral-temporal feature) is strongly dependant on the DM that is used to dedisperse a dynamic spectrum, and since the DM of a source varies from burst to burst as well as with time, we studied the variation of our drift and duration measurements for each burst at different choices of DM. Dedispersion can be performed by optimizing signal-to-noise (S/N) or by optimizing a structure parameter and can result in very different values found for the DM depending on the burst (e.g. Fig 1 of Gajjar et al. 2018). In particular, an algorithm seeking to choose a DM by maximizing S/N might stack the components of a complex bursts and yield a DM value that is higher than a structure optimizing algorithm. For bursts with components that are not clearly resolved it becomes ambiguous which algorithm is most accurate and the precision in the DMs determined burst to burst can be much narrower than the variations in the DM observed overall for a source (CHIME/FRB et al. 2020). It therefore becomes difficult to uncouple FRB characteristics from the nature of the medium in order to study relationships between spectral-temporal features as we hope to do. One option is to use the DM found along with its high precision on a burst by burst basis, however doing this can become a complicated process of verifying that the DM algorithm choice is appropriate, which will often be ambiguous for smeared bursts where it is not clear if it consists of multiple components or not. Without a detailed understanding of the emission mechanism, the medium, the source, and the resulting DM distribution as a function of time, it is in fact much simpler and more conservative to choose a DM range as wide as possible based on the history of DMs found for the source. We shall see that despite the huge errors this choice entails, the data still points to the existence of an inverse trend between the sub-burst drift and the burst duration for the three sources considered here.

Table 1 shows the DM ranges chosen for each source and dataset, in each case aiming to consider as broad a range of DMs as possible while still obtaining reasonable sub-drift rate measurements. For the data used from Michilli et al. 2018 dispersion measure variations are believed by those authors to be $\lesssim 1\%$ of 559.7 pc/cm^3 so we assume that 1% variation is possible and compute a range of 554.1–565.3 pc/cm^3 to use. For the data from Gajjar et al. 2018, due to availability, we use the sub-bursts in burst 11A

Source	Data	DM Range(pc/cm ³)
FRB121102	Michilli et al. 2018	554.1-565.3
FRB121102	Gajjar et al. 2018	555-570 (555-583)
FRB180916.J0158+65	CHIME/FRB et al. 2020	346.82-349.82
FRB180814.J0422+73	CHIME/FRB et al. 2019	188.7-190.0

Table 1. The range of DMs used to determine the range of possible values of each burst's sub-drift rate and duration. These are chosen to be as large as possible while still obtaining reasonable sub-drift rate measurements based on the errors. In general, the range of DMs observed burst-to-burst determines the range used, with some DMs on the higher end excluded due to distortion observed when dedispersing to those DMs. See the text for more details.

and burst 11D. A structure optimized DM for 11A is found at 565 pc/cm³, and their figure 1 indicates that DMs between 555-570 are also close to optimal, so we adopt this range. For burst 11D, due to a lack of structure we adopt a range of 555-583 to be closer to its S/N optimized DM, however higher DMs are excluded as the drift rates start to become positive (which are not physical according to our model and in general usually indicate too aggressive of a de-dispersion). For data from CHIME/FRB et al. 2020 an extremely precise DM of 348.82 ± 0.05 pc/cm³ is found for one of the bursts, but burst-to-burst the DM can range from 348.7-350.2. We roughly center about 348.82 pc/cm³ and adopt a range of 346.82-349.82 pc/cm³. The lower value for the start of the range is to push the limit of acceptable DMs while still obtaining reasonable drift rate measurements while we stay away from the higher end of the observed range due to the distortion and positive drift rates observed for most of the bursts at that high of a DM. Finally, for data from CHIME/FRB et al. 2019, due to the structure present in the bursts, we adopt the full range of structure optimized DMs found (188.9-190 pc/cm³) but expand the lower end and use 188.7-190 pc/cm³. We ignore the higher S/N optimized DMs due to the component stacking and distortion observed when de-dispersing to those DMs.

For each source, we generate a grid of DMs over the DM range chosen and dedisperse each burst to each DM before performing an auto-correlation analysis. The grid spacing varies from $\Delta\text{DM} \approx 0.1\text{-}2$ pc/cm³ depending on the source, yielding roughly 10-20 trial DMs in each case. For bursts with multiple components like burst 11A from Gajjar et al. 2018, the components are separated manually by finding valleys in the corresponding time series of the data. When possible these components are padded with a background sample of the burst in order to protect from array looping during dedispersion. Some bursts are not clearly resolved, but wherever there is indication that the sub-drift suddenly changes mid-burst a manual attempt is made to separate the components.

The autocorrelation analysis is then performed for each dedispersed waterfall and yields sub-drift rate and duration measurements for each burst at each DM, and we use this data to determine the range of possible values for each measurement. The range for each of these measurements is found to be much larger than the parameter error from the underlying 2d gaussian fit, indicating that the covariance between the measurements and the DM is larger than with the model parameters. Since the underlying DM distribution for each source must so far be narrower than the DM range we've used (considering the distribution so far implied by published DMs

and knowing that the distribution can change with time), the range of values found this way must be larger than the range implied by the true error bars for each measurement. We therefore treat the range of values found by this analysis as upper-limit estimates of the real measurement errors.

2.2 Burst Exclusions and Fitting

With the measurements for each burst at each trial DM found, there remain measurements that are unconstrained and/or assumed to be non-physical that need to be discarded before fitting. In particular, we discard any positive sub-drift rate measurements following the assumption of our model that these are artificial, and measurements where the value and/or error approaches infinite, as is the case for bursts that become near vertical or circular in their autocorrelation. Circular, 'blobby' bursts tend to have a large error associated with their fit parameters, while vertical but otherwise elliptically shaped autocorrelations suggest that a slightly lower DM might be closer to the true DM.

The result of this exclusion process is that for most of the bursts in our sample, we retain all the measurements made over the DM ranges specified in Table 1. For bursts that have had measurements excluded, we automatically limit the DM range further (in every case except one by lowering the maximum trial DM) to keep the drift rate measurement negative. We could choose to exclude these bursts completely from the sample however we find that our conclusion remains the same. We therefore instead mark them specially in the key figures to come to indicate the higher possibility of an unconstrained measurement. For all but one of the bursts treated this way, the DM range is only slightly restricted to achieve meaningful drift rate measurements and still spans more than half the original range. For one burst from FRB180814, the DM range is limited more aggressively from 188.7 - 190.0 pc/cm³ to 188.8 - 188.9 pc/cm³.

Using this set of measurements we find a fit to equation (1) at each DM for each source. We choose an optimal DM for each source that represents the "best case scenario" of fits (ie. assuming that the three sources should obey the same law), and use the range of fits found to indicate where the fit can possibly be for the range of DMs considered. The optimal DMs found for each source were 559.7 and 565 pc/cm³ for the data from Michilli et al. 2018 and Gajjar et al. 2018, respectively, and 348.82, and 188.9 pc/cm³ for FRB180916 and FRB180814, values that are all within the DM ranges chosen previously.

3 RESULTS

We show in Figure 1 the results of our analysis, where the sub-burst drift rate (normalized to the frequency of observation ν_{obs}) is plotted against the temporal width t_w for the three FRBs. Normalizing the sub-burst drift has the advantage of allowing us to combine the different sources on the same graph irrespective of the frequency of observation, shifts due to the dynamical Doppler effect or cosmological redshift. Furthermore, we note that equation (1) is also insensitive to temporal scaling transformations. For example, interstellar scintillation, which brings a temporal broadening scaling inversely with the fourth power of the frequency, will have no effect on our analysis. The only consequence being a shift of data points along the specific law characterized by the parameter A in equation (1). The points displayed in Figure 1 are the measurements of each

burst obtained at the optimal DM described at the end of Section 2.2, and the capped lines represent the range of possible measurements for that burst over the DM range considered.

Examination of Figure 1 reveals that the inverse relationship between the two parameters is clearly seen for all sources on the graph for values ranging over two orders of magnitude for both the normalized sub-burst drift rate and the temporal duration. Also shown in the figure are fits for the predicted function A/t_w (see equation (1)) for the three sources independently, with $A = 0.085 \pm 0.006$, 0.081 ± 0.006 and 0.079 ± 0.014 for FRB 121102, FRB 180916.J0158+65 and FRB 180814.J0422+73, respectively. These fits represent the strongest possible conclusion that the three sources obey precisely the same law. The shaded regions for each source represent the variety of fits found when considering all DMs in the possible range, and show the range of possible fits. The range of possible fit parameters are found to be $A = 0.041 - 0.355$, for FRB 121102, $A = 0.030 - 0.267$ for FRB 180916.J0158+65, and $A = 0.079 - 0.240$ for FRB 180814.J0422+73. These regions overlap significantly, but indicate the possibility of unique and distinct fits between the three sources. We note that the range for FRB 180814.J0422+73 is completely contained in either of the other two ranges.

A few important consequences are to be noted from the results presented in Figure 1. First, we consider the strongest possible conclusion that not only is the inverse relationship between the sub-burst drift and duration verified for the three sources, but they do so with similar values for A in equation (1). The different fits to this systemic parameter are similar given their uncertainties, and it is difficult to visually distinguish between the corresponding curves. This closeness between the values obtained for A is rather remarkable and suggests the existence of a single and common underlying physical phenomenon responsible for the emission of FRB signals in the three sources. This is significant because these FRBs are associated with different types of host galaxies at various redshifts. More precisely, FRB 121102 is localized to a low-metallicity irregular dwarf galaxy at a redshift $z = 0.193$ (Tendulkar et al. 2017), while the redshift of FRB 180814.J0422+73 is estimated to be $z \leq 0.1$ (CHIME/FRB et al. 2019). Furthermore, the candidates for the host galaxy of FRB 180814.J0422+73 are not consistent with those harboring long gamma-ray bursts (LGRBs) or superluminous supernovae (SLSNe), unlike the host galaxy of FRB 121102 (Li et al. 2019). As for FRB 180916.J0158+65, it is precisely localized to a star-forming region in a massive spiral galaxy at a redshift $z = 0.0337$ (Marcote et al. 2020). This source is the closest known extragalactic FRB, whose host galaxy does not show signatures of a strong magnetic field nor a radio counterpart as reported for FRB 121102.

Other than the conclusion that the three sources obey the same law, there are other related inferences that can be made given these results and in light of the difficulty in constraining the measurements of the burst properties. Even with the large ranges of measurements seen, Figure 1 strongly suggests each source likely obeys a form of equation (1), where we see a clear decrease in the magnitude of drift rates with increasing burst duration. We interpret the large overlap between the possible fit regions as an indication that it is likely that these sources obey the same type of law, but that distinct parameters for each source are possible. Several of the bursts from FRB180814.J0422+73 lie close to but outside their region of possible fits and the narrow DM range required to constrain burst

measurements for this source may be due to the small bandwidths observed for the bursts available, which increases the error associated with the sub-drift rate measurement.

As was discussed in Rajabi et al. (2020), the three predictions made by our simple dynamical model (i.e., the narrowing of sub-bursts width t_w with increasing frequency ν_{obs} , the sad or happy trombone effect and the sub-burst drift law discussed here) provide strong evidence that the underlying physical phenomenon is narrow-band in nature. This is because the dependencies on ν_{obs} and the frequency of emission in the FRB rest frames ν_0 for the three predicted relationships are such that it would be difficult to envision how they could be realized through the data if ν_0 was allowed to vary substantially (see the SM for more details). Although data over a significant range of observed frequency is currently only available for FRB 121102 (and constitutes the basis of the analysis presented in Rajabi et al. 2020), the fact that FRB 180916.J0158+65 and FRB 180814.J0422+73 follow the same law renders it reasonable to expect that the conclusions reached for FRB 121102 also apply to them.

We can use this information with our model to further characterise the environment of the sources responsible for the detected bursts. Indeed using the extensive data available for FRB 121102 one can estimate, although with limited precision at this point, the maximum Lorentz factor and the rest frame frequency of emission ν_0 . To do so we will assume highly simplified conditions, i.e., that the different FRB reference frames from which the sub-bursts emanate either move towards or away from the observers with the same range of speeds. We will denote by $\beta^+ > 0$ and $\beta^- = -\beta^+$ the maximum velocities (divided by the speed of light) towards and away from the observer, respectively, with corresponding observed frequencies ν_{obs}^\pm . It is then straightforward to show that, under this assumption,

$$\beta^+ = \frac{\nu_{\text{obs}}^+ - \nu_{\text{obs}}^-}{\nu_{\text{obs}}^+ + \nu_{\text{obs}}^-} \quad (2)$$

$$\nu_0^2 = \nu_{\text{obs}}^+ \nu_{\text{obs}}^- \quad (3)$$

Using $\nu_{\text{obs}}^+ \simeq 7.5$ GHz and $\nu_{\text{obs}}^- \simeq 630$ MHz we find $\beta^+ \approx 0.9$ and $\nu_0 \approx 2.6$ GHz for FRB 121102 (taking into account its known redshift $z = 0.193$ from Tendulkar et al. 2017; see the SM for more details). Evidently, the accuracy for these estimates is set and limited by the frequency coverage of the existing data and is likely to change as more detections are acquired. For example, confirming the purported detection of signals at 111 MHz from Fedorova & Rodin (2019) would further increase β^+ and bring down ν_0 on the order of 1 GHz. At any rate, these results imply that FRB 121102 is potentially very strongly relativistic.

We also know that the spectral width $\Delta\nu_{\text{obs}}$ associated to sub-bursts for FRB 121102 scales as $\Delta\nu_{\text{obs}} \sim 0.16 \nu_{\text{obs}}$ (see Figure 6 in Rajabi et al. 2020 or Figure 5 in Houde et al. 2019). This spectral extent is the result of motions within a given FRB rest frame from where a sub-burst centred at ν_{obs} originates. As discussed in the SM section, the observed spectral width is constrained through

$$2\Delta\beta' \leq \frac{\Delta\nu_{\text{obs}}}{\nu_{\text{obs}}} \leq \frac{2\Delta\beta'}{1 - \Delta\beta'^2}, \quad (4)$$

where the motions in the FRB rest frame are contained within $\pm\Delta\beta'$. We thus find $\Delta\beta' \sim 0.08$ with equation (4) for this source.

We thus have a picture where FRB 121102 and similar sources would consist of systems within which a number of spatially distinct FRB rest frames, whose motions cover a wide range of velocities (some highly relativistic relative to the observer), are responsible for

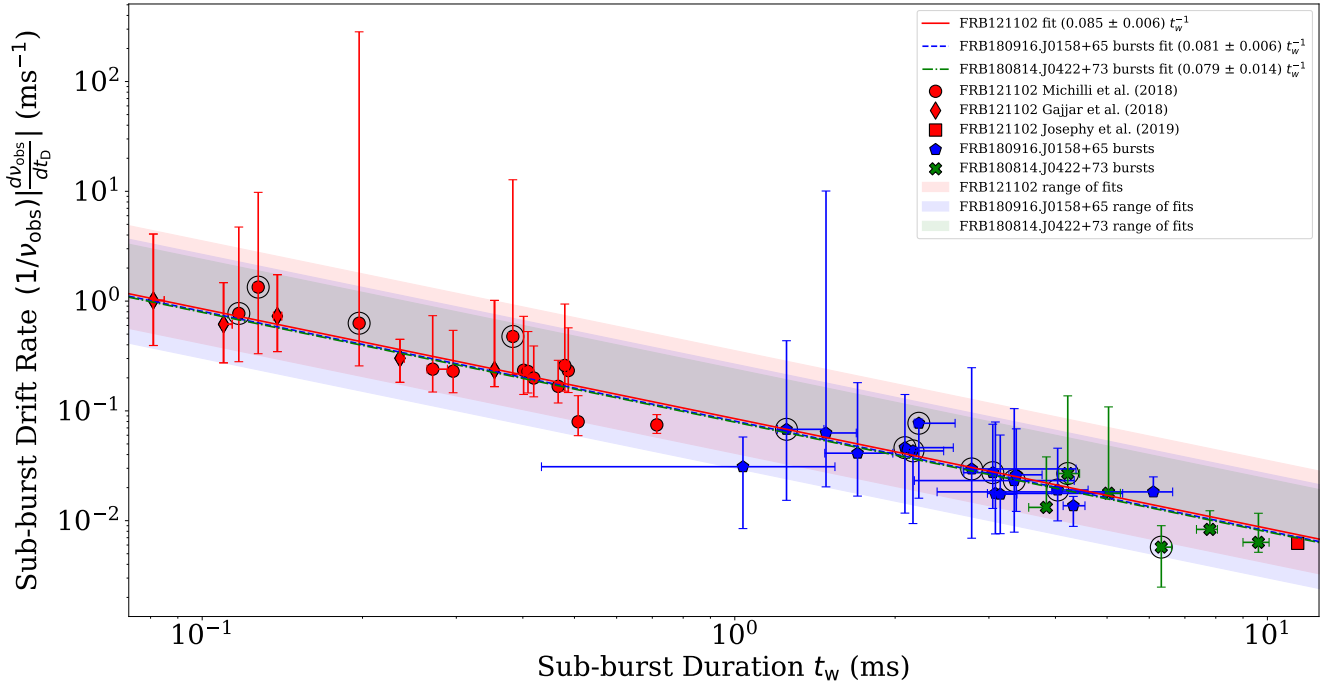


Figure 1. A plot of $(1/\nu_{\text{obs}}) |d\nu_{\text{obs}}/dt_D|$ vs. t_w for bursts from FRB 121102 (red circles, diamonds and square; Gajjar et al. 2018; Michilli et al. 2018; Josephy et al. 2019), FRB 180916.J0158+65 (blue pentagons; CHIME/FRB et al. 2020) and FRB 180814.J0422+73 (green crosses; CHIME/FRB et al. 2019). The sub-burst drift $d\nu_{\text{obs}}/dt_D$ and duration t_w were obtained using the two-dimensional autocorrelation technique of Hessels et al. (2019), while the center frequency ν_{obs} was estimated from the corresponding dynamic spectra. Each burst was dedispersed to a grid of trial DMs over the range specified by Table 1 and the measurements were repeated. The points displayed are of measurements made at an ‘optimal’ DM within that range that represents the case where the three sources obey the same fit. The red, blue and green lines are for fits of the function A/t_w on the ‘optimal’ FRB 121102, FRB 180916.J0158+65 and FRB 180814.J0422+73 data, respectively, and are difficult to distinguish from one another. The capped lines at each point represent the range of possible measurements obtained via the autocorrelation analysis for different DMs over the DM ranges chosen. As discussed in Section 2.1, these are used in lieu of the difficult to determine true measurement errors but are necessarily larger than the true errors, and can be interpreted as a proxy for the measurement error introduced by DM uncertainty. The circled points indicate the bursts that required a more limited DM range to constrain their measurements (see Section 2.2). The shaded regions represent the range of fits found when using measurements obtained at other DMs in the range, and represents the range of possible fits. These regions overlap significantly, but indicate the possibility of unique and distinct fits between the three sources within the range of possible DMs chosen.

the emission of individual sub-bursts. In turn, each such rest frame is also host to mildly relativistic motions, which are responsible for the observed wide spectral widths of sub-bursts.

Finally, we note that our discovery of a shared sub-burst drift law among these three sources suggests that this could be a universal property among repeating FRBs or at least a significant subclass of them. This not only motivates further searches but also provides a new tool to study and categorize FRBs based on their underlying physical mechanism.

4 DISCUSSION: MEASURING BURST PROPERTIES

We discuss here the process of preparing and obtaining measurements from the dynamic spectra of bursts, based on the autocorrelation technique described in Hessels et al. (2019). We also discuss the effects of noise on the measurement of the sub-drift rate and the burst duration as well as the effect of the DM variations on the autocorrelation of dynamic spectra.

As mentioned in Section 2.1 when a dynamic spectrum consists of a train of multiple sub-bursts we separate the components and measure the drift rate and duration of each sub-burst separately.

The dynamic spectra of every burst used in this analysis with its autocorrelation is shown in Figures 6 – 10.

The pipeline that every sub-burst undergoes is written in Python and consists of computing the autocorrelation of the signal, fitting a two-dimensional (2D) Gaussian to the resulting autocorrelation function, and a calculation of the physical quantities of interest from the fit parameters: namely the sub-burst drift rate and duration. The autocorrelation of the dynamic spectrum measures the self-similarity of the sub-burst in frequency-time space and for FRBs can be approximated by an ellipsoid with an intensity that follows a 2D Gaussian (Hessels et al. 2019). Before computing the autocorrelation and depending on the source and/or burst, some noise removal is performed. For the bursts from FRB 121102 and FRB 180916.J0158+65 this is done by subtracting from the entire spectrum a background signal obtained from a time-average of twenty or so samples taken prior to the burst. For FRB 180814.J0422+73, due to the raw format the bursts are provided in, a noise mask was acquired through correspondence with members of the CHIME/FRB Collaboration and the channels are normalized by the standard deviation of the intensity. Missing or blocked out frequency channels in dynamic spectra (e.g., because of radio frequency interference (RFI)) are zeroed out before performing the autocorrelation.

The computation of the autocorrelation function is facilitated and sped up by using a Fast Fourier Transform (FFT) of the dynamic spectrum, which is then squared and inverted (through an FFT) back to the frequency-time domain (Press et al. 2007). The autocorrelation function is then modelled with the following functional form for a rotated 2D Gaussian

$$G(x, y) = C \exp \left\{ -\frac{1}{2} \left[x^2 \left(\frac{\cos^2 \theta}{b^2} + \frac{\sin^2 \theta}{a^2} \right) + 2xy \sin \theta \cos \theta \left(\frac{1}{b^2} - \frac{1}{a^2} \right) + y^2 \left(\frac{\sin^2 \theta}{b^2} + \frac{\cos^2 \theta}{a^2} \right) \right] \right\}, \quad (5)$$

with the free parameters C , a , b , and θ for, respectively, the amplitude, the semi-major and semi-minor axes (i.e., the standard deviations) of the ellipsoid, and the sub-drift angle for the orientation of the semi-major axis measured counterclockwise from the positive y -axis. More precisely, the x - (i.e., for the time lag) and y -axes (i.e., for the frequency lag) are respectively oriented horizontally and vertically on the autocorrelation plots shown in Figures 6–10 below. To find these parameters we use the `scipy.optimize.curve_fit` package, which performs a non-linear least squares fit. The package also returns a covariance matrix, which is used to calculate the uncertainty of the fitted parameters. These uncertainties are then scaled by the square-root of the reduced χ^2 computed from the residual between the autocorrelation function and its Gaussian fit. We note again that the uncertainty calculated this way does not capture nearly the entire error budget which depends more significantly on the error in the DM (discussed in Section 2.1) as well the parts of the burst spectra that have been masked out and the shape of its autocorrelation.

Using the angle θ , the sub-burst drift rate is calculated via

$$\frac{dv_{\text{obs}}}{dt_D} = -\frac{\nu_{\text{res}}}{t_{\text{res}}} \cot \theta, \quad (6)$$

where ν_{res} and t_{res} are the frequency and time resolutions of the dynamic spectrum. We obtain the sub-burst duration from the fit parameters through

$$t_w = t_{\text{res}} \frac{ab}{\sqrt{b^2 \sin^2 \theta + a^2 \cos^2 \theta}}. \quad (7)$$

These expressions are also used to propagate the fit parameter uncertainties to the values of dv_{obs}/dt_D and t_w . These uncertainties are used to confirm the claim that DM variations are the largest source of error, as stated in Section 2.1.

The observation frequency ν_{obs} of each burst is estimated via an intensity-weighted average of the spectrum over the whole time range. While this decreases the accuracy of the estimate as opposed to using just the on-pulse region, we find it has little bearing on the result. To fit equation (1) we used the `scipy.odr.RealData` package, which uses orthogonal distance regression and uses the uncertainties on the data to find a fit. We use the range of measurements obtained over the range of trial DMs as the uncertainty when performing this fit.

4.1 DM Variations as a Rotation of the ACF

Based on the study of the variation of measurements over ranges of plausible DMs discussed in 2.1, different DM choices can be seen as rotations of the autocorrelation function of the burst. As an example, we show in Figure 2 two bursts each at two choices of DM.

In the burst waterfall we see that the shape of the burst can appear to ‘distort’ due to the ν^{-2} dependence of dispersion, while the shape of the burst’s autocorrelation remains the same while experiencing a rotation. To characterize this further we consider the angle parameter (as opposed to the drift rate derived from said angle) found for the bursts from FRB 180916.J0158+65 against the burst duration derived from the underlying 2d gaussian fit in Figure 3. This shows that across different DMs the measured duration varies little while the angle found is offset from angles at other DMs by a constant angle. We can demonstrate this using equations (1) and (6) to find that the drift angle is related to the sub-burst duration through

$$\theta = \arctan \left(\frac{1}{A} \frac{\nu_{\text{res}}}{\nu_{\text{obs}}} \frac{t_w}{t_{\text{res}}} \right), \quad (8)$$

where as before $A \equiv \tau_w'/\tau_D'$. We also approximated ν_{obs} to be constant, which is adequate for this purpose. We find that the chosen fit obtained with equation (8) for the sub-bursts at $\Delta\text{DM} = 0$ (i.e., the solid curve in Figure 3) is also satisfactory for angles corresponding to the different ΔDM values when a simple offset angle (i.e. a rotation) is applied. Similar trends appear to hold for the other two sources considered, however it is most clear in the example of FRB 180916.J0158+65.

Considering the angle instead of the drift rate during analysis at first appears to avoid the discontinuity in drift rate measurements around $\theta = 0, \pi$, or where the drift rate approaches infinity. If one were not making the assumption that positive drift rates were nonphysical, then the angle might be the measurement of interest. However, since we wish to impose the constraints of negative drift rates as well as a constrained uncertainty on the measurement, a discontinuity near angles that lead to nearly vertical drift rate still exists. The behaviour of drift rate measurements derived from the parameter angle in the context of autocorrelation noise is discussed in more detail in Pleunis (2020) as well as in the `dfdt`¹ package.

4.2 Error Introduced by Frequency Band Masking

As noted in Section 4, we first transformed our dynamic spectra via the 2D autocorrelation technique introduced in Hessels et al. (2019), and then extracted the sub-burst drift (dv_{obs}/dt_D) and temporal duration (t_w) via a Gaussian fit optimization procedure. In addition to random signal noise, the dynamic spectra analyzed were complicated by missing frequency bands of data, which would sometimes overlap with the frequency extent of the sub-burst under analysis. In this section we assess the error introduced by the missing frequency band data by (1) artificially masking (zero-padding) various trial Gaussian signals of known orientations and characteristic widths, (2) processing them through our pipeline, and (3) comparing the extracted sub-burst drift and duration parameters to the generating parameters.

Consider for example burst 23 (B23) of FRB 180916.J0158+65 (CHIME/FRB et al. 2020) pictured, along with its two-dimensional autocorrelation, in Figure 8. Three frequency bands of data are absent from the original data in B23, and the total missing bandwidth (as a fraction of the frequency extent of the sub-burst) is higher than the fractional bandwidth typically absent from sub-bursts analyzed in the paper. We therefore treat B23 as representative of a higher-than-average measure of frequency band masking error.

To estimate the effect of missing frequency channels on our analysis we construct an artificial burst from a Gaussian of $a =$

¹ <https://github.com/zpleunis/dfdt>

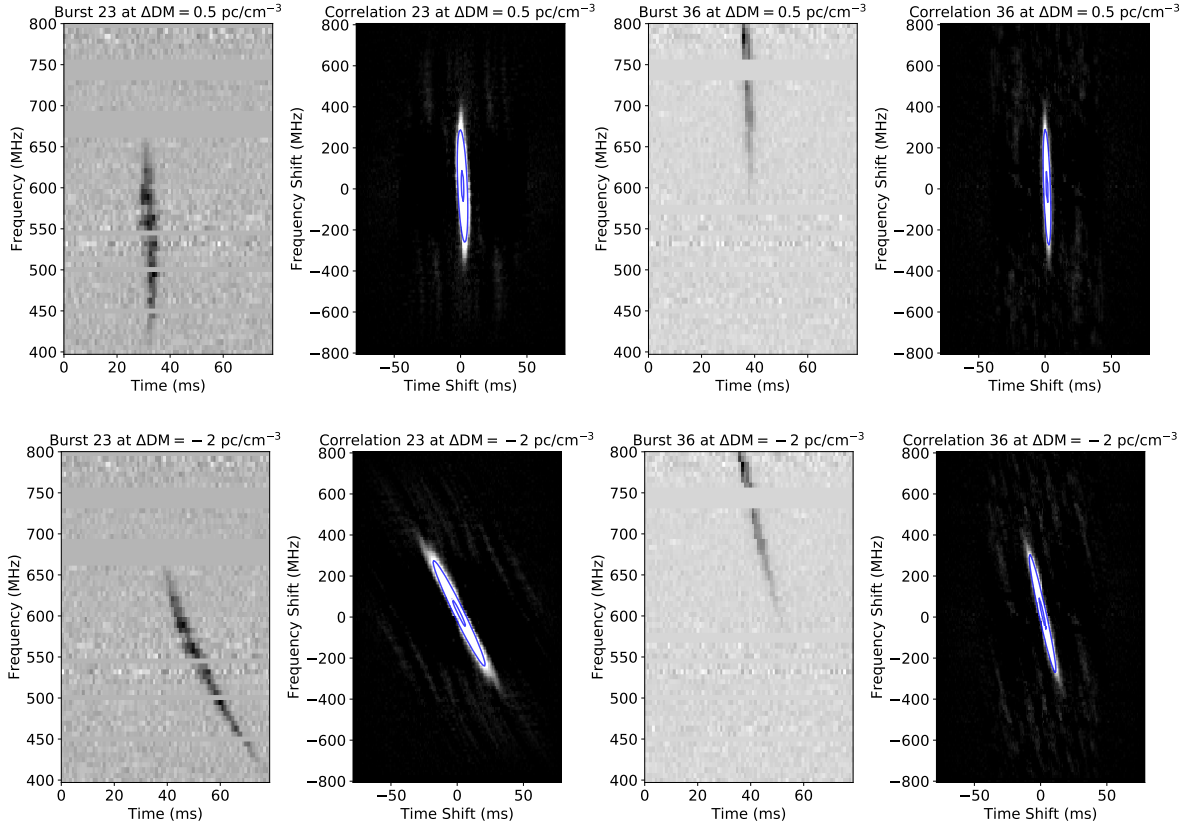


Figure 2. Changes to dynamic spectra and autocorrelation as a function of variations in the DM. Sub-bursts 23 (first column) and 36 (third column) from FRB 180916.J0158+65 are shown with their autocorrelation functions (second and fourth columns, respectively) for two offsets $\Delta\text{DM} = 0.5 \text{ pc cm}^{-3}$ (top row) and -2 pc cm^{-3} (bottom row) from the ‘optimal’ value chosen for our analysis (i.e., $\text{DM} = 348.82 \text{ pc cm}^{-3}$). The rotations brought about by the small changes in DM are clearly seen in both the dynamic spectra and autocorrelation functions.

67 MHz (90 pixels), $b = 2.2 \text{ ms}$ (15 pixels), $\theta = 10^\circ$ (inclination from vertical), and with stochastic noise of amplitude 25% that of the Gaussian amplitude. We perform our analysis on a 2D image with dimensions 540×540 (W×H) pixels, having horizontal and vertical resolutions of 6.75 pixels/ms and 1.35 pixels/MHz respectively. As a first test, we mask a band of 18.5 MHz (25 pixels) on the Gaussian’s vertical centre and pass this zero-padded signal through our pipeline. This Gaussian geometry and mask bandwidth are representative of B23.

The fitting procedure on the 2D autocorrelation returns $a_{\text{fit}} = 102.7$ pixels, $b_{\text{fit}} = 14.8$ pixels, and $\theta_{\text{fit}} = 9.83^\circ$. The process is visualized in Figure 4. For such a small inclination angle, the percentage error in τ_w is very close to that of b , and is (in this case) approximately 1%. The percentage error in the sub-burst drift $d\nu_{\text{obs}}/d\tau$ is

$$\left| \frac{\Delta(d\nu_{\text{obs}}/d\tau)}{d\nu_{\text{obs}}/d\tau} \right| 100\% = \left| \frac{\tan(9.83^\circ) - \tan(10.0^\circ)}{\tan(10.0^\circ)} \right| 100\% \quad (9)$$

$$= 1.7\%. \quad (10)$$

We can generalize this test by shifting the frequency masking band of Figure 4 vertically. Upon doing so, we find that the error is independent of the frequency band’s vertical position. The percentage error for the pulse duration is found to be $\approx (-1.4 \pm 0.4)\%$, where the $\pm 0.4\%$ uncertainty applies to all band vertical positions tested, while the corresponding error in the angle is $\approx (-1.1 \pm 0.7)\%$.

If we further rotate the pulse of Figure 4, while retaining the

central band mask of 18.5 MHz (25 pixels) on pulse centre, we observe a linear enhancement of error with increasing orientation. The effect is, however, a negligible one: for every pulse rotation by 10° , the duration error increases by only 0.45%, while the orientation angle error decreases (or increases in magnitude) by only 0.12° . **At a 30.0° pulse angle, the sub-burst drift error is only 4%.**

5 DISCUSSION: THE NARROW-BAND NATURE OF THE EMISSION PROCESS

Following the model of Rajabi et al. (2020), the temporal duration of an FRB sub-burst in the observer rest frame is given by

$$t_w = \tau'_w \frac{\nu_0}{\nu_{\text{obs}}}, \quad (11)$$

where, as defined in Section 1.1, τ'_w , ν_0 and ν_{obs} respectively are the proper temporal width and frequency of emission in the FRB rest frame, and the frequency of the signal as measured by the observer. Equation (11) clearly predicts an inverse relationship between the observed FRB temporal width and frequency, which had previously been noticed and studied. For example, a verification of this effect can be found in Figure 7(b) of Gajjar et al. (2018) for the case of FRB 121102. Although the burst temporal duration exhibits a fair amount of scattering at a given frequency (inherent to τ'_w in equation (11)), the predicted behavior is clearly observed. Since the data used for this source come from observations spanning a wide range of

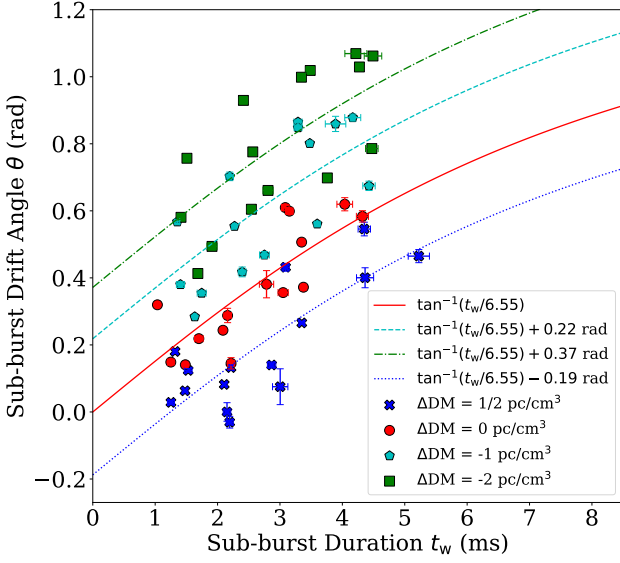


Figure 3. The fit angle θ vs. sub-burst duration t_w from bursts de-dispersed to small variations in the DM for the source FRB 180916.J0158+65. Red circles are sub-bursts at $\Delta\text{DM} = 0$ which corresponds to a DM = 348.82 pc cm⁻³. Blue crosses, cyan pentagons, and green squares are sub-bursts de-dispersed to $\Delta\text{DM} = 0.5, -1$, and -2 pc cm⁻³, respectively. Error bars indicate the parameter fitting error. The red curve is fit to the red circles and is of the form given in equation (8), derived from the dynamical model described in the main text. Blue, cyan, and green curves are obtained by adding a rotation (i.e., adding an angle) to the $\Delta\text{DM} = 0$ model. As discussed in Section 4.1 this plot demonstrates the rotational effect small variations in the DM can have on the autocorrelation of dynamic spectra of FRBs.

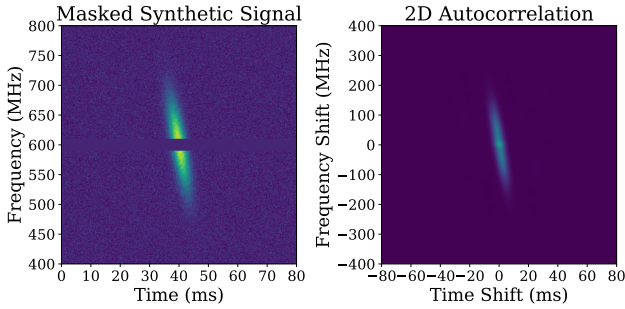


Figure 4. Synthetic Gaussian signal with a masked (zeroed) band (left), and 2D autocorrelation of masked signal (right). The signal shown approximately matches the characteristics of Burst 23 depicted in Figure 8 in each of their temporal widths, their frequency extents, their inclinations, and their total missing frequency bandwidths.

frequencies, it further follows from equation (11) that the rest frame frequency ν_0 cannot change significantly as a function of ν_{obs} , as this would affect the inverse relationship observed in the data.

Rajabi et al. (2020) also derived the following equation for the drift in the observed central frequency of a sequence of sub-bursts with increasing arrival time

$$\frac{\Delta\nu_{\text{obs}}}{\Delta t_D} = \frac{\nu_{\text{obs}}}{\nu_0} \frac{d\nu_{\text{obs}}}{d\tau'_D}, \quad (12)$$

where the term on the left-hand side is for the central frequency drift and τ'_D is the proper temporal delay between the arrival of the trigger and the emission of the ensuing sub-burst in the FRB rest frame.

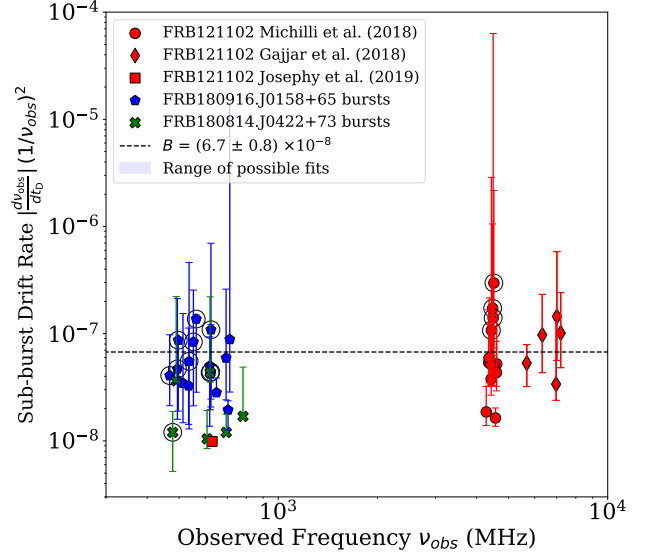


Figure 5. A plot of $(1/\nu_{\text{obs}}^2) |d\nu_{\text{obs}}/d\tau'_D|$ vs. ν_{obs} for FRB 121102 (red circles, diamonds and square from Gajjar et al. 2018, Michilli et al. 2018 and Josephy et al. 2019, respectively), FRB 180916.J0158+65 (blue pentagons; CHIME/FRB et al. 2020) and FRB 180814.J0422+73 (green crosses; CHIME/FRB et al. 2019). The broken black line is for a fit to a constant B on the combined data for the three sources, with $B \equiv (\tau'_D \nu_0)^{-1} = (6.7 \pm 0.8) \times 10^{-8}$. The capped lines at each point represent the range of possible values due to the range of sub-drifts measured at different DMs, as discussed in Section 2.1. These are used in lieu of the unknown true measurement errors but are necessarily larger than the true errors. The shaded region indicates the range of possible fits for the constant B when accounting for the range of possible sub-drift values and ranges from 2.1×10^{-8} to 3.5×10^{-6} .

The derivative $d\nu_{\text{obs}}/d\tau'_D$ is a physical parameter characterizing the environment of the FRB source, which determines whether the sequence of sub-bursts has the appearance of a “sad” ($d\nu_{\text{obs}}/d\tau'_D < 0$) or “happy trombone” ($d\nu_{\text{obs}}/d\tau'_D > 0$; see Rajabi et al. 2020 for more details). Equation (12) predicts that the central frequency drift should scale linearly with ν_{obs} , which has previously been verified for FRB 121102 over a wide range of frequencies. This can be asserted, for example, from Figure 3 (top panels) of Hessels et al. (2019). Once again, this observed dependency could not be realized if ν_0 changed significantly in equation (12).

Finally, equation (11) can be inserted in equation (1) of the main text to obtain

$$\frac{1}{\nu_{\text{obs}}^2} \frac{d\nu_{\text{obs}}}{d\tau'_D} = -\frac{1}{\nu_0 \tau'_D}, \quad (13)$$

for the sub-burst drift (normalized to ν_{obs}^2), which is then predicted to be independent of ν_{obs} and scale inversely with ν_0 . Figure 5 shows the corresponding plot using the same data as in Figure 1. The broken black line is for a fit to a constant B on the combined data for the three sources, with $B \equiv (\tau'_D \nu_0)^{-1} = (6.7 \pm 0.8) \times 10^{-8}$. While there is some scatter in the data, the expected lack of dependency with ν_{obs} is observed. any deviation can easily be accounted for with the uncertainty on the DMs. As was the case for the temporal narrowing and sad trombone effect discussed above for FRB 121102, this behavior would be affected if ν_0 changed significantly in equation (13).

Taken together the verification of these three predictions provide strong evidence that the underlying physical process responsible for the emission of FRB signals in these repeating FRBs is narrow-band in nature.

5.1 Determination of β^+ , ν_0 and $\Delta\beta'$

The equations presented in this section apply to cases where the source of radiation travels directly toward or away from the observer.

For the determination of the maximum speed of an FRB rest frame toward the observer $\beta^+ > 0$ and ν_0 , the frequency of emission within it, we can generally set $\beta^- = -a\beta^+$ with $a \geq 0$ for the greatest (i.e., most negative) speed away from the observer. Using the relativistic Doppler shift formula (Rybicki & Lightman 1979) for the corresponding frequencies in the observer's rest frame

$$\nu_{\text{obs}}^{\pm} = \nu_0 \sqrt{\frac{1 + \beta^{\pm}}{1 - \beta^{\pm}}}, \quad (14)$$

we find that

$$\beta^+ = \left(\frac{1+a}{2a} \right) \left(\frac{\nu_{\text{obs}}^{+2} + \nu_{\text{obs}}^{-2}}{\nu_{\text{obs}}^{+2} - \nu_{\text{obs}}^{-2}} \right) \times \left[1 - \sqrt{1 - \frac{4a}{(1+a)^2} \left(\frac{\nu_{\text{obs}}^{+2} - \nu_{\text{obs}}^{-2}}{\nu_{\text{obs}}^{+2} + \nu_{\text{obs}}^{-2}} \right)^2} \right] \quad (15)$$

$$\nu_0^2 = \nu_{\text{obs}}^+ \nu_{\text{obs}}^- \sqrt{\frac{1 - (1-a)\beta^+ - a\beta^{+2}}{1 + (1-a)\beta^+ - a\beta^{+2}}}. \quad (16)$$

The discussion in Section 3 where the FRB rest frames span the range $\pm\beta^+$ corresponds to the case $a = 1$, which reduces equations (15)–(16) to equations (2)–(3) of the main text. We also note that a system becomes most strongly relativistic when $a \rightarrow 0$ where $\nu_0 \rightarrow \nu_{\text{obs}}^-$, while the opposite is true as $a \rightarrow \infty$ and $\nu_0 \rightarrow \nu_{\text{obs}}^+$.

For the determination of $\Delta\beta'$, we start by considering that for a signal initially observed at frequency ν_{obs} a velocity change $\Delta\beta$ in the observer's rest frame will be accompanied by a change $\delta\nu_{\text{obs}}$ in frequency given by

$$\frac{\delta\nu_{\text{obs}}}{\nu_{\text{obs}}} = \frac{\Delta\beta}{1 - \beta^2}, \quad (17)$$

where β is the initial velocity relative to the observer. Using the special relativistic velocity addition law (Rybicki & Lightman 1979) we can relate the velocity changes in the observer and FRB rest frames through

$$\Delta\beta = \Delta\beta' \left(\frac{1 - \beta^2}{1 + \beta\Delta\beta'} \right), \quad (18)$$

with $\Delta\beta'$ the corresponding velocity change in the FRB frame.

Allowing for the motions within the FRB rest frame to span the range $\pm\Delta\beta'$ (with $\Delta\beta' \geq 0$; for simplicity, we assume a symmetric velocity range about zero), while using equations (14) (to express β as a function of ν_{obs} and ν_0) and (17)–(18), we find the following relation for the total observed bandwidth covered by the corresponding signals

$$\frac{\Delta\nu_{\text{obs}}}{\nu_{\text{obs}}} = 2\Delta\beta' \left[1 - \Delta\beta'^2 \left(\frac{\nu_{\text{obs}}^2 - \nu_0^2}{\nu_{\text{obs}}^2 + \nu_0^2} \right)^2 \right]^{-1}. \quad (19)$$

Equation (4) follows from this relation, which reaches a maximum

value when $\nu_{\text{obs}} = 0$ or $\nu_{\text{obs}} \gg \nu_0$. While equation (19) shows little variations whenever $\Delta\beta' \ll 1$, it could, in principle, be used to evaluate the FRB rest frame frequency ν_0 independently of equation (16) since it reaches a minimum of $2\Delta\beta'$ at $\nu_{\text{obs}} = \nu_0$. However, the effect is probably too small (on the order of 1% for FRB 121102) to be measurable given the scatter inherent to FRB data.

6 CONCLUSION

We demonstrate a method of studying the difficult to measure sub-drift rate in the context of DM variations from burst to burst and over time by adopting large ranges of possible DMs when measuring spectro-temporal properties of FRBs. This method reveals that even given a wide range of possible DMs for each burst from an FRB source, the sub-drift rate of an individual FRB is inversely proportional to its duration. Furthermore, for the three sources considered in this work, namely FRB 121102, FRB 180916.J0158+65 and FRB 180814.J0422+73, significant overlap between the inverse trends found is consistent with the three relationships having a nearly identical scaling; that is, the same law can be used to describe bursts from all three sources, though a more careful treatment of each burst's DM would be needed to prove this.

We believe that the simplest explanation for the existence of this trend is that the emission mechanism of these FRB sources is narrow-band in nature, and that if indeed multiple sources obey the same scaling of the law, then a single line transition may be responsible for the FRB phenomenon through, for example, Dicke's superradiance. Such a mechanism requires a trigger, which leaves room for magnetar-centric models of FRBs within the context of this result. To study this relationship further future analysis of FRBs from all known repeater sources can be performed to test the hypothesis that all FRB repeaters can be characterized by such an inverse law. A large sample of sources helps to constrain the error due to variations in DM, and necessitates convenient and public access to FRB data.

If deviations from this relationship exist, then it is likely the sub-drift law can serve as a classification tool for FRB sources by discriminating sources that follow this law from those that do not.

ACKNOWLEDGEMENTS

The authors are grateful to Z. Pleunis and S. Tendulkar from the CHIME/FRB Collaboration for their help in accessing and analyzing the data for FRB 180916.J0158+65 and FRB 180814.J0422+73. M.H. is grateful for the hospitality of Perimeter Institute where part of this work was carried out. M.H.'s research is funded through the Natural Sciences and Engineering Research Council of Canada Discovery Grant RGPIN-2016-04460. F.R.'s research at Perimeter Institute is supported in part by the Government of Canada through the Department of Innovation, Science and Economic Development Canada and by the Province of Ontario through the Ministry of Economic Development, Job Creation and Trade. F.R. is in part financially supported by the Institute for Quantum Computing. C.M.W. and A.M. are supported by the Natural Sciences and Engineering Research Council of Canada (NSERC) through the doctoral post-graduate scholarship (PGS D).

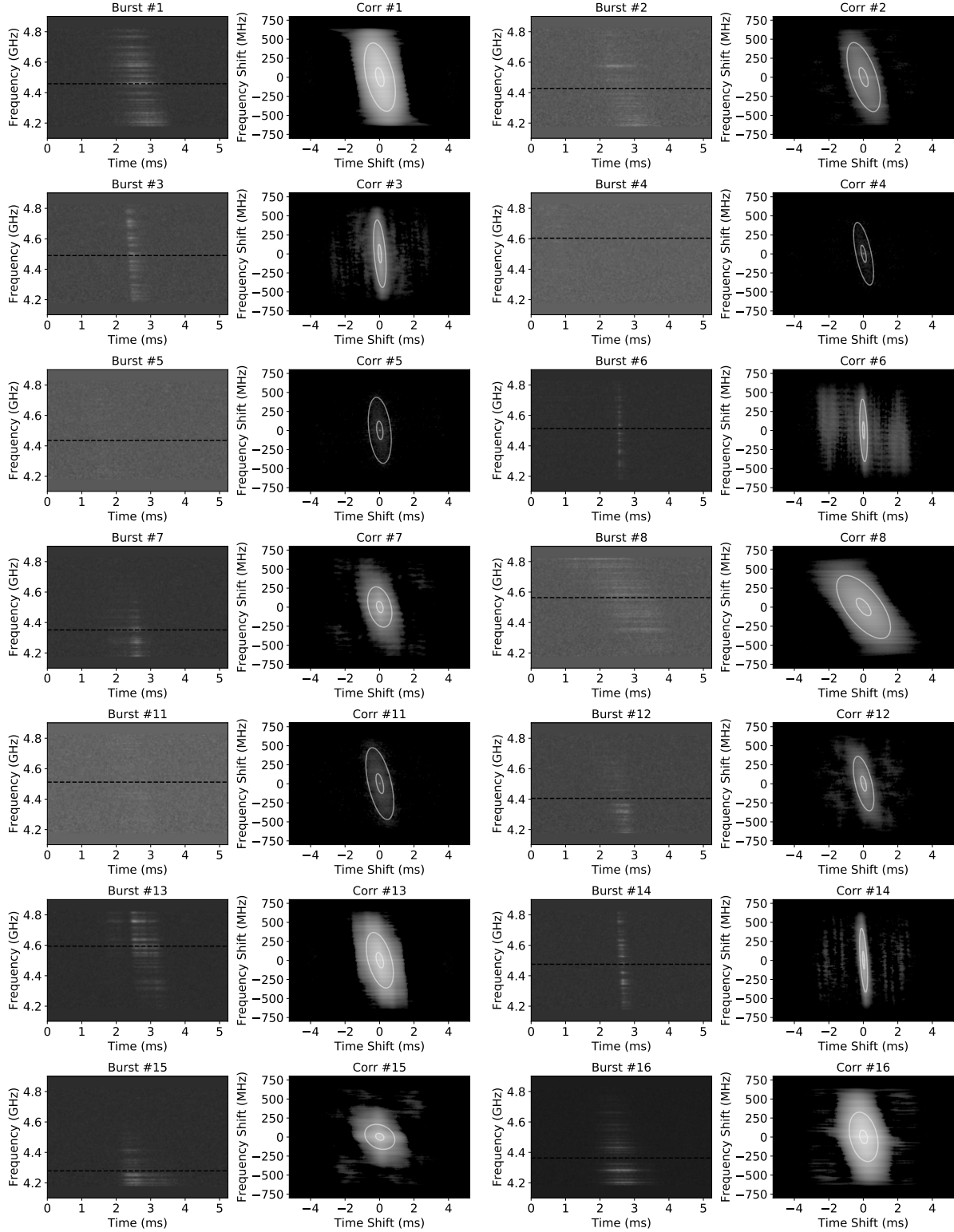


Figure 6. Dynamic spectra (first and third columns) and corresponding autocorrelation functions (second and fourth columns) for FRB 121102 bursts at a frequency of approximately 4–5 GHz from [Michilli et al. \(2018\)](#). The dynamic spectra were de-dispersed with a $DM = 559.7 \text{ pc cm}^{-3}$ and the dashed horizontal line in the dynamic spectra denotes the center frequency ν_{obs} used for the analysis. The autocorrelation functions are modelled with a 2D Gaussian ellipsoid whose one- and two-standard deviation levels are shown using the white contours.

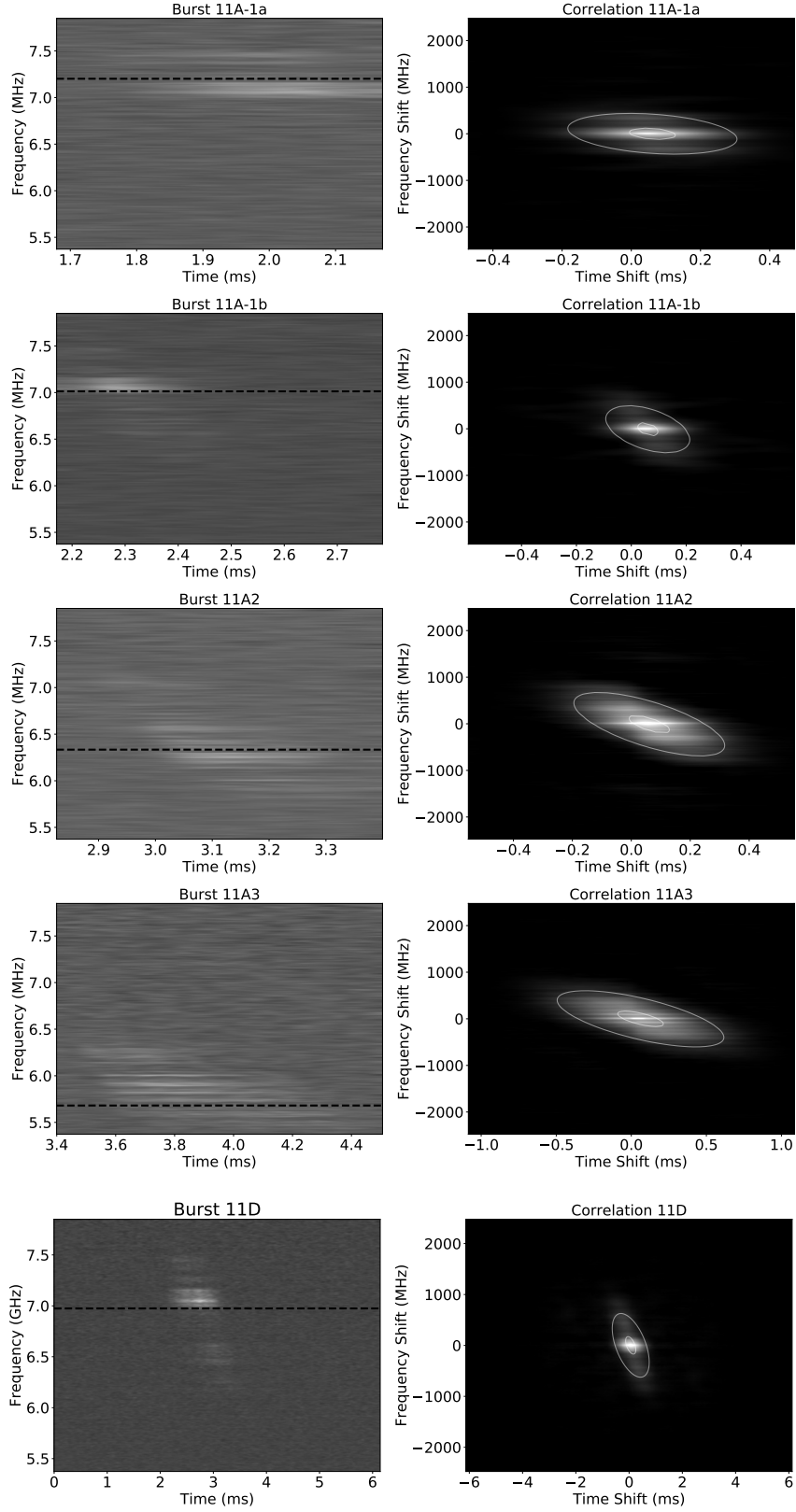


Figure 7. Same as Figure 6 but for the FRB 121102 data at approximately 5–8 GHz published in [Gajjar et al. \(2018\)](#) and de-dispersed with a $DM = 565 \text{ pc cm}^{-3}$. The top four sub-bursts are taken from one event, i.e., Burst 11A. Note that the time axes for the autocorrelation functions do not all share the same range, which distorts their relative appearance.

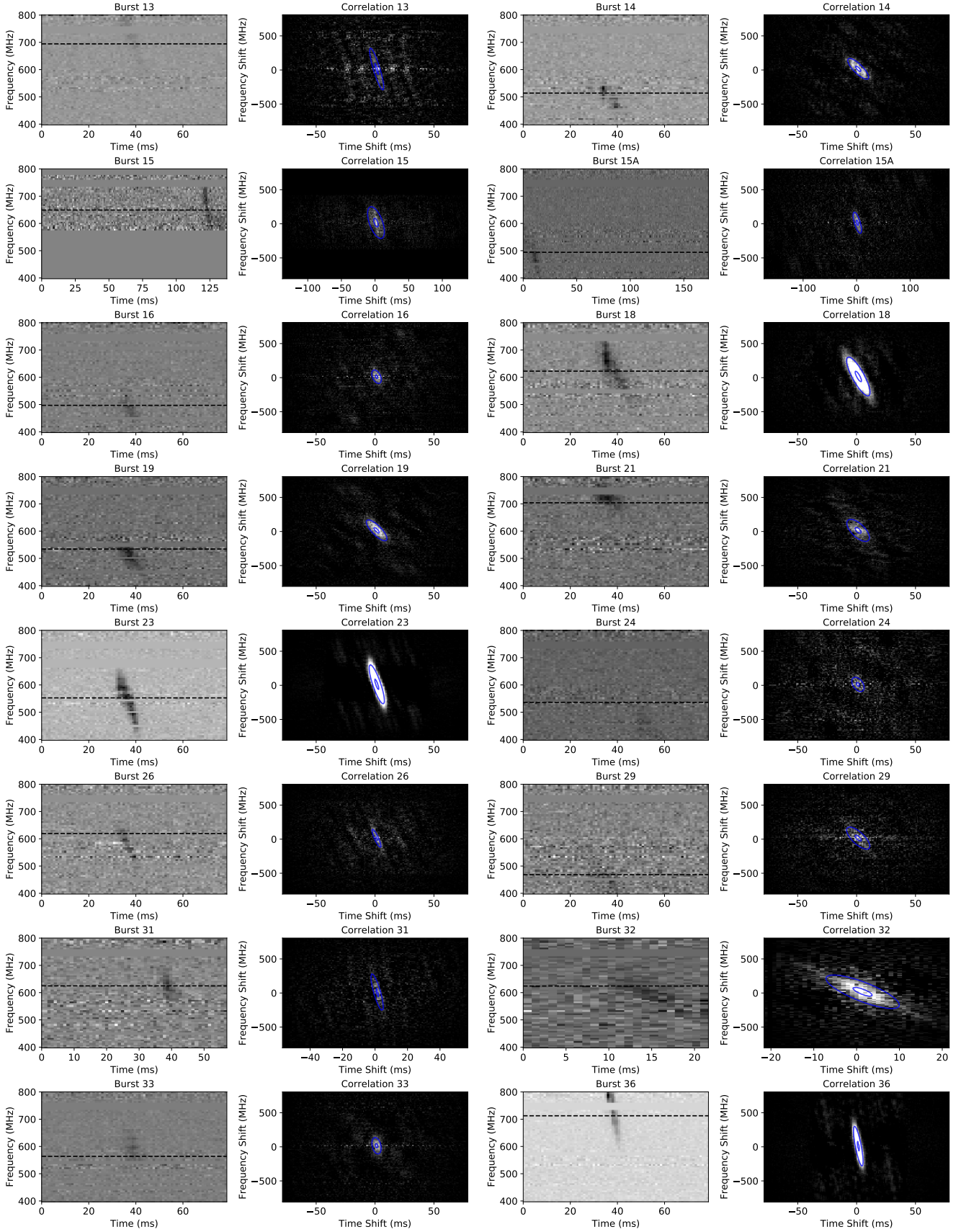


Figure 8. Same as Figure 6 but for FRB 180916.J0158+65 taken from CHIME/FRB et al. (2020). These data were de-dispersed with a $DM = 348.82 \text{ pc cm}^{-3}$. Note that the time axes for the autocorrelation functions do not all share the same range, which distorts their relative appearance.

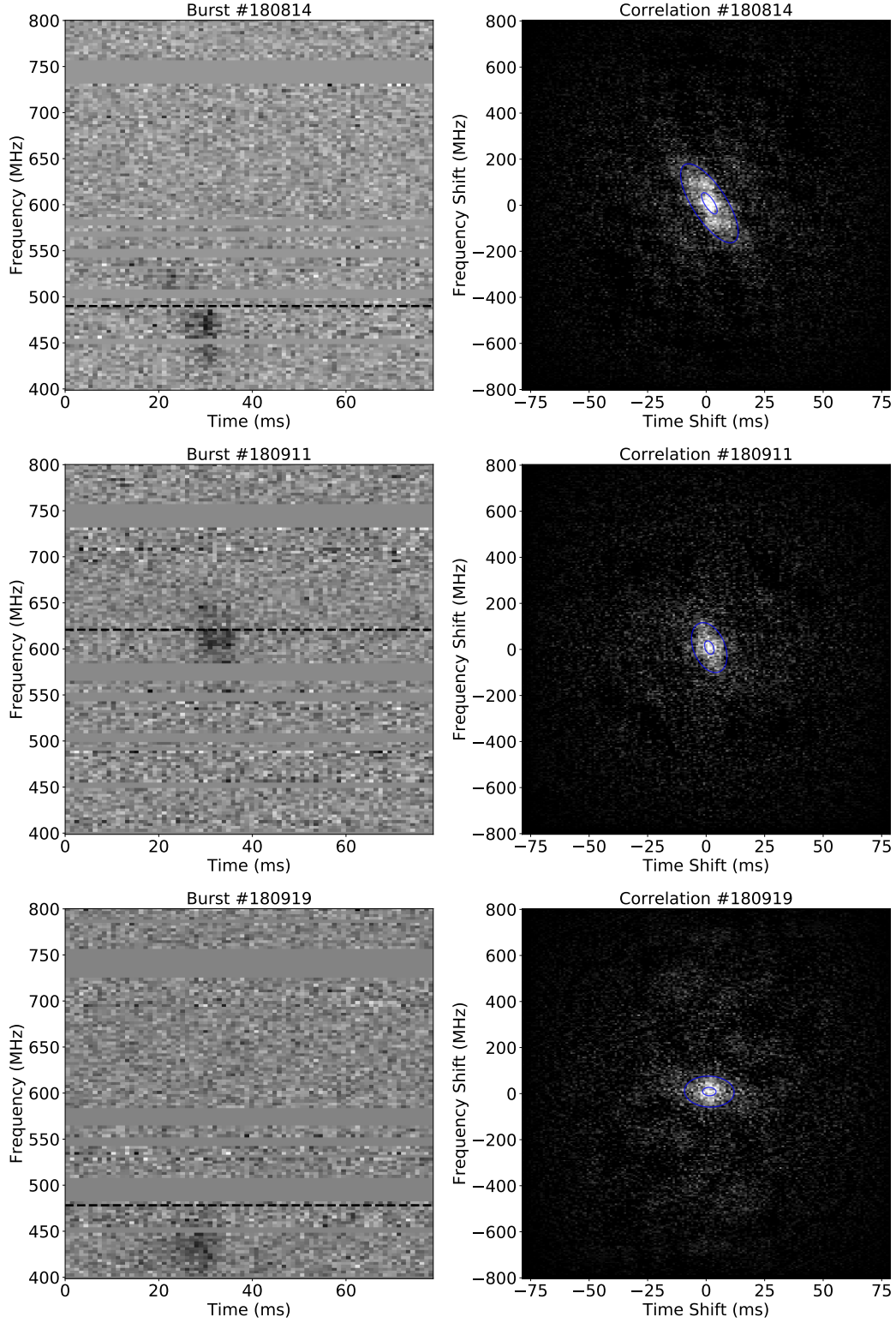


Figure 9. Same as Figure 6 but for FRB 180814.J0422+73 taken from [CHIME/FRB et al. \(2019\)](#). These data were de-dispersed with a $DM = 188.9 \text{ pc cm}^{-3}$.

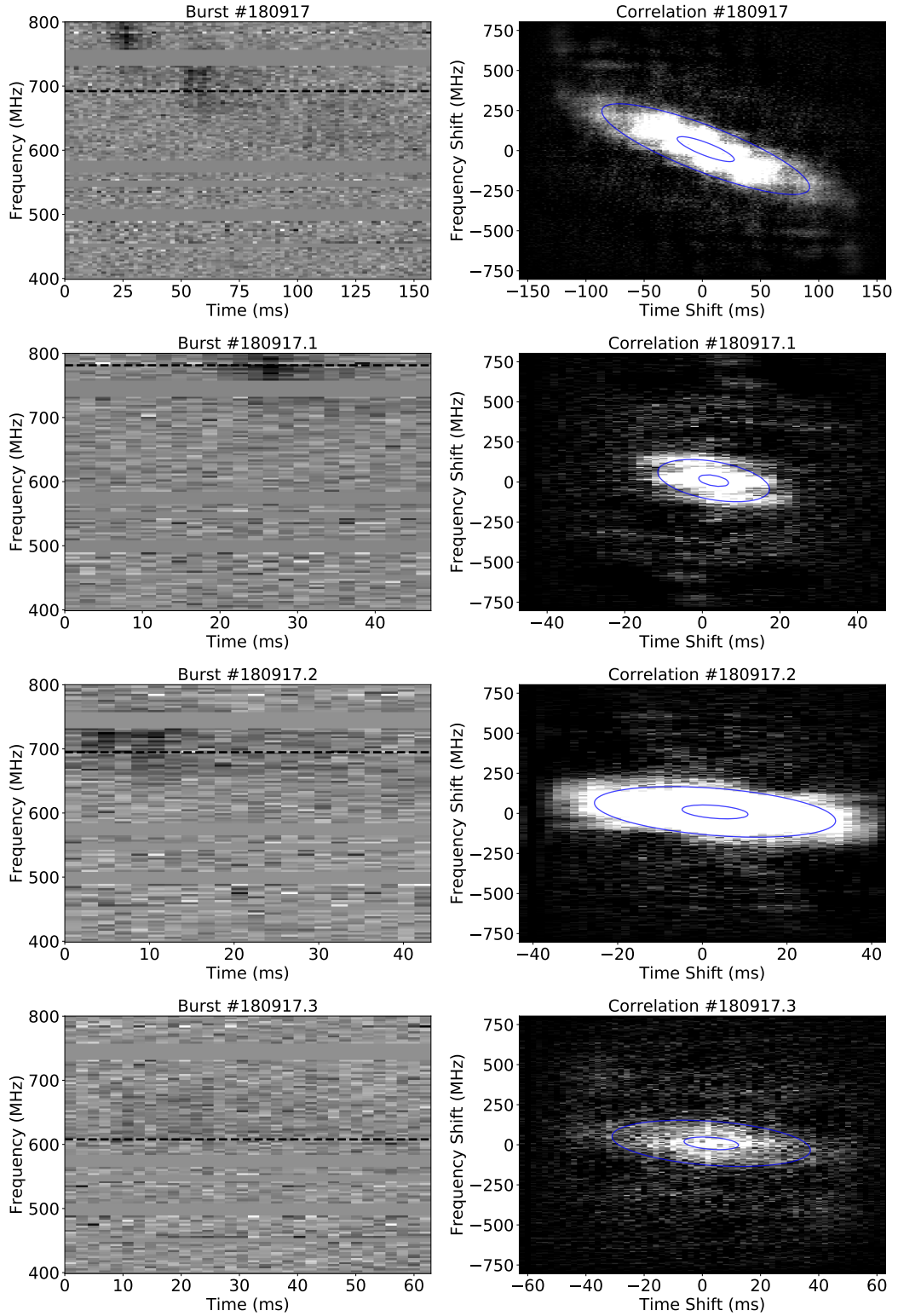


Figure 10. Same as Figure 9 but for Burst #180917 of FRB 180814.J0422+73 taken from [CHIME/FRB et al. \(2019\)](#). The whole event is shown on the top row (not used for Figure 1 of main text), while its three separate sub-bursts are detailed in the bottom three (all used for Figure 1 of main text). Note that the time axes for the autocorrelation functions do not all share the same range, which distorts their relative appearance.

DATA AVAILABILITY STATEMENT

The data pipeline is made available at <https://github.com/mef51/subdriftlaw> and maintained by M.A.C. Aggregate data of the bursts and the code for the figures are also available. Data of the FRB spectra are available either publicly or via the authors of their respective publications. The figures in this paper were prepared using the matplotlib package (Hunter 2007).

REFERENCES

- Beloborodov A. M., 2020, *ApJ*, 896, 142
- Beniamini P., Kumar P., 2020, *MNRAS*, 498, 651
- Bochenek C. D., Ravi V., Belov K. V., Hallinan G., Kocz J., Kulkarni S. R., McKenna D. L., 2020, *Nature*, 587, 59
- CHIME/FRB Collaboration Andersen B., et al., 2019, *ApJ*, 885, L24
- CHIME/FRB et al., 2019, *Nature*, 566, 235
- CHIME/FRB Amiri M., et al., 2020, *Nature*, 582, 351
- Cordes J. M., Wasserman I., Hessels J. W. T., Lazio T. J. W., Chatterjee S., Wharton R. S., 2017, *ApJ*, 842, 35
- Fedorova V. A., Rodin A. E., 2019, *Astron. Rep.*, 63, 39
- Fonseca E., et al., 2020, *ApJ*, 891, L6
- Gajjar V., et al., 2018, *ApJ*, 863, 2
- Hessels J. W. T., et al., 2019, *ApJ*, 876, L23
- Houde M., Mathews A., Rajabi F., 2018, *MNRAS*, 475, 514
- Houde M., Rajabi F., Gaensler B. M., Mathews A., Tranchant V., 2019, *MNRAS*, 482, 5492
- Hunter J. D., 2007, *Computing in Science & Engineering*, 9, 90
- Joseph A., et al., 2019, *ApJ*, 882, L18
- Kirsten F., Snelders M. P., Jenkins M., Nimmo K., van den Eijnden J., Hessels J. W. T., Gawroński M. P., Yang J., 2020, *Nature Astronomy*, 6, 100
- Li Y., Zhang B., Nagamine K., Shi J., 2019, *ApJ*, 884, L26
- Lorimer D. R., Bailes M., McLaughlin M. A., Narkevic D. J., Crawford F., 2007, *Science*, 318, 777
- Marcote B., et al., 2020, *Nature*, 577, 190
- Mathews A., 2017, The Role of Superradiance in Cosmic Fast Radio Bursts, Honours thesis, The University of Western Ontario
- Metzger B. D., Margalit B., Sironi L., 2019, *MNRAS*, 485, 4091
- Michilli D., et al., 2018, *Nature*, 553, 182
- Petroff E., Hessels J., Lorimer D., 2019, *A&ARv*, 27, 4
- Pleunis Z., 2020, PhD thesis, McGill University
- Press W. H., Teukolsky S. A., Vetterling W. T., Flannery B. P., 2007, Numerical Recipes 3rd Edition: The Art of Scientific Computing, 3 edn. Cambridge University Press, USA
- Rajabi F., Houde M., 2016a, *ApJ*, 826, 216
- Rajabi F., Houde M., 2016b, *ApJ*, 828, 57
- Rajabi F., Houde M., 2017, *Sci. Adv.*, 3, e1601858
- Rajabi F., Houde M., 2020, *MNRAS*, 494, 5194
- Rajabi F., Houde M., Bartkiewicz A., Olech M., Szymczak M., Wolak P., 2019, *MNRAS*, 484, 1590
- Rajabi F., Chamma M. A., Wyenberg C. M., Mathews A., Houde M., 2020, *MNRAS*, 498, 4936
- Rajwade K., et al., 2020, *MNRAS*, 495, 3551
- Rybicki G. B., Lightman A. P., 1979, Radiative processes in astrophysics. New York: Wiley
- Simard D., Ravi V., 2020, *ApJ*, 899, L21
- Tendulkar S. P., et al., 2017, *ApJ*, 834, L7
- The CHIME/FRB Collaboration Andersen B. C., et al., 2020, *Nature*, 587, 54
- Wang W., Zhang B., Chen X., Xu R., 2019, *ApJ*, 876, L15

This paper has been typeset from a \LaTeX file prepared by the author.